HOMOGENISED LIMIT ANALYSIS OF MASONRY WALLS.
PART II: STRUCTURAL EXAMPLES

G.MILANI[1*], P.B.LOURENÇO[2], A.TRALLI[1]

[1] *Faculty of Engineering, University of Ferrara, Via Saragat 1, 44100-Ferrara (IT)*
[2] *Department of Civil Engineering, School of Engineering, University of Minho, Azurém, 4800 Guimarães (PT)*

ABSTRACT

The homogenised failure surfaces obtained through the simple micro-mechanical model developed in the first part of the paper are here used for the analysis of in-plane loaded masonry walls. Both upper and lower bound homogenised limit analyses are employed for treating meaningful structural cases, namely a deep beam and a set of shear walls. Detailed comparisons between the experimental data and numerical results obtained using both a heterogeneous and a homogenised approach are also presented. The examples show the efficiency of the homogenised technique with respect to: 1) accuracy of the results; 2) reduced number of finite elements required; 3) independence of the mesh, at a structural level, from the actual texture of masonry. A final example on a large scale wall is presented with the aim to show an engineering application of the proposed approach.

Keywords: masonry, homogenisation, limit analysis, shear walls, finite element analysis

---

[*] Corresponding Author. Dipartimento di Ingegneria – Università degli Studi di Ferrara – Via Saragat 1 – 44100 – Ferrara - Italy. e-mail: gmilani@ing.unife.it . Phone: +39 0532 974911. Fax: +39 0532 974870.

1 INTRODUCTION

The evaluation of the ultimate load bearing capacity of large scale walls under horizontal and vertical loads is a fundamental task for the design of masonry structures. Although in the past several models for the analysis of the brickwork have been proposed, the approach based on the use of averaged constitutive equations for masonry seems to be the only one suitable to be employed in a large scale finite element analysis [1], [2].

From a practical viewpoint, in fact, a heterogeneous approach based on micro-modelling seems to be limited to the study of panels of small dimensions, due to the large number of variables involved in a non linear finite element analysis. Therefore, alternative strategies based on macro-modelling have been recently developed in order to tackle engineering problems. As already discussed in the companion paper (part I), a drawback of macro-approaches is the mechanical characterisation of the model, which is essentially derived from experimental data fitting [3]. Obviously, this means that the introduction of new materials and/or the application of a well known material in different loading conditions might require a different set of experimental programs on masonry specimens.

On the other hand, the homogenisation technique seems to be a very powerful tool for the analysis of large scale masonry structures, because mechanical properties of constituent materials and geometry of the elementary cell are taken into account only at a cell level. In this way, large scale walls can be analysed through standard finite element codes without direct representation of the micro-mechanical properties of the cell, such as texture, thickness, geometry of units and mechanical characteristics of components. Furthermore, the application of homogenisation theory to the rigid-plastic case [4] [5] requires only a reduced number of material parameters and provides, from an engineering viewpoint, important information at failure, such as limit multipliers of loads, collapse mechanisms and, at least on critical sections, the stress distribution [6]. For the above

reasons, homogenisation combined with limit analysis seems to be an efficient tool for the ultimate analysis of large scale masonry structures.

Nevertheless, a typical drawback of this approach is its inability to predict displacements at the collapse. Moreover, an infinite plastic deformation capacity of the material at hand is assumed: this hypothesis should be checked case by case, depending on the geometry of the masonry wall and on the distribution of loads applied. In particular, masonry walls exhibiting rocking failure modes or shear failure modes present usually a significantly ductile behaviour.

In this paper, a homogenised finite element limit analysis is discussed in detail and applied to several examples of technical relevance. Both upper and lower bound approaches are developed, with the aim to provide a complete set of numerical data for the design and/or the structural assessment of complex structures. The finite element lower bound analysis is based on the equilibrated triangular element by Sloan [7], while the upper bound is based on a modified version of the triangular element with discontinuities of the velocity field in the interfaces by Sloan and Kleeman [8]. The modification takes into account the actual shape of the yield surface for the homogenised material in the interfaces.

The paper is organised as follows: in Section 2, a concise review of the finite element lower bound approach is reported, whereas in Section 3 the upper bound modified triangular element with jump of velocities in interfaces is discussed. Some meaningful structural examples are treated in detail in Section 4, concerning a deep beam [9] and a set of shear walls [10]. The reliability of the homogenised approach is assessed through a comparison with experimental results and a heterogeneous approach recently presented in the literature [11]. Finally, in Section 5, the analysis of an existing structure [12] is discussed in detail, with the aim of showing the possibilities and the reliability of the proposed model in comparison with other approaches. In the Appendix, the mesh

dependence of the results, both for the upper and the lower bound elements, is discussed, using one of the examples reported in the text.

2   THE LOWER BOUND APPROACH

For the lower bound approach, a complete 2D finite element limit analysis program based on the equilibrated triangular element by Sloan [7] has been implemented using Matlab™. The triangular element, used to model the stress field under plane stress, is shown in Figure 1. The variation of stresses throughout each element is linear. Differently from the elements used in displacement finite element analysis, in a limit analysis program several nodes may share the same coordinate, being each node associated with only one element. In this way, statically admissible stress discontinuities can occur at shared edges between adjacent triangles. Denoting by N_E the number of triangles in the mesh, the number of nodes is $3N_E$ and $9N_E$ are the total unknown stresses (three stresses per node, namely Σ_{xx}, Σ_{yy} and Σ_{xy}). The nine unknown stress parameters of the element have to fulfil internal equilibrium conditions, which lead to two equations per element (formulated in the x and y directions). Furthermore, additional constraints on the nodal stresses at the edges of adjacent triangles are imposed in order to secure interfacial equilibrium. With this aim, the continuity of the shear and normal components of the stress tensor between adjacent elements is imposed, i.e. the stress vector on the edges of the triangle is preserved passing from a goven element to the neighbouring element.

Following [13], the previous conditions of equilibrium and admissible discontinuities for an element can be given, in compact notation, as follows:

$$\mathbf{q} = \mathbf{H}\widetilde{\boldsymbol{\Sigma}} \tag{1}$$

Eq. (1) represents the equilibrium equation for the homogenised material and corresponds to Eq. (7a) and (9a) of the companion paper (Part I), which have been written for the microscopic quantities. Eq. (1) collects both equilibrium inside an element and the shear and normal stresses (expressed in terms of the 9 unknown stresses of the element) on the three edges of the triangle (Figure 1). The terms involved more are given more as follows:

1) $\mathbf{H}$ is a 14×9 equilibrium matrix and reads:

$$\mathbf{H} = \begin{bmatrix} \mathbf{h}_1 & \mathbf{0} & \mathbf{0} \\ \mathbf{0} & \mathbf{h}_2 & \mathbf{0} \\ \mathbf{0} & \mathbf{0} & \mathbf{h}_3 \\ \mathbf{h}_1^{M} & \mathbf{h}_2^{M} & \mathbf{h}_3^{M} \end{bmatrix}$$

(2)

where $\mathbf{h}_r$ and $\mathbf{h}_r^{M}$ ($r = 1,\ldots,3$) are defined in item 4 below).

2) $\mathbf{q}$ takes the role of vector of nodal forces and reads:

$$\mathbf{q} = \begin{bmatrix} \mathbf{q}_1 & \mathbf{q}_2 & \mathbf{q}_3 & \mathbf{q}_1^{M} + \mathbf{q}_2^{M} + \mathbf{q}_3^{M} \end{bmatrix}^{T}$$

(3)

The involved $\mathbf{q_i}$ vectors are:

- the 4×1 interface stress vectors $\mathbf{q}_1\ \mathbf{q}_2\ \mathbf{q}_3$, one for each node of the element. In particular $q_r = \begin{bmatrix} q_{2\sigma}^{j} & q_{2\tau}^{j} & q_{1\sigma}^{k} & q_{1\tau}^{k} \end{bmatrix}^{T}$, with $r = 1,2,3$ $j = 3,1,2$ and $k = 2,3,1$ (see also Figure 1) represents the shear and normal stresses of edges j, k of the triangle calculated on node r;

- the 2×1 vectors $\mathbf{q}_r^{M}$, which represent the contribution of the 3 stress parameters of node r to the internal equilibrium of the element ($div\mathbf{\Sigma} + \mathbf{b} = \mathbf{0}$, with $\mathbf{b} = \mathbf{0}$, see Figure 1). Obviously, being the stress shape functions linear, the internal equilibrium of each element is satisfied imposing the equilibrium, for instance in the barycentre M (or in any other point) of the element.

3) the 9×1 vector $\tilde{\mathbf{\Sigma}}$, which represents the vector of element unknowns:

$$\tilde{\Sigma} = \begin{bmatrix} \Sigma^{(1)} & \Sigma^{(2)} & \Sigma^{(3)} \end{bmatrix}^T \tag{4}$$

and collects the 3x1 vectors of nodal stress parameters $\Sigma^{(r)}$ ($\Sigma^{(r)} = \begin{bmatrix} \Sigma_{xx}^{(r)} & \Sigma_{yy}^{(r)} & \Sigma_{xy}^{(r)} \end{bmatrix}^T$, $r = 1,2,3$).

4) matrices $\mathbf{h}_r$ and $\mathbf{h}_r^{\mathrm{M}}$, which depend only on the geometry of the element. Assuming r with values ($r = 1,2,3$), with A the area of the triangular element and with x, y the coordinates of the nodes, $\mathbf{h}_r$ and $\mathbf{h}_r^{\mathrm{M}}$ are given by the following expressions:

$$\mathbf{h}_r = \begin{bmatrix} \dfrac{(y_k - y_r)^2}{l_{kr}^2} & \dfrac{(x_k - x_r)^2}{l_{kr}^2} & -2\dfrac{(x_k - x_r)(y_k - y_r)}{l_{kr}^2} \\[2mm] \dfrac{(x_k - x_r)(y_k - y_r)}{l_{kr}^2} & -\dfrac{(x_k - x_r)(y_k - y_r)}{l_{kr}^2} & \dfrac{(y_k - y_r)^2 - (x_k - x_r)^2}{l_{kr}^2} \\[2mm] \dfrac{(y_r - y_j)^2}{l_{rj}^2} & \dfrac{(x_r - x_j)^2}{l_{rj}^2} & -2\dfrac{(x_r - x_j)(y_r - y_j)}{l_{rj}^2} \\[2mm] \dfrac{(x_r - x_j)(y_r - y_j)}{l_{rj}^2} & -\dfrac{(x_r - x_j)(y_r - y_j)}{l_{rj}^2} & \dfrac{(y_r - y_j)^2 - (x_r - x_j)^2}{l_{rj}^2} \end{bmatrix}$$

$$\mathbf{q}_r = \begin{bmatrix} q_{2\sigma}^j \\ q_{2\tau}^j \\ q_{1\sigma}^k \\ q_{1\tau}^k \end{bmatrix} = \mathbf{h}_r \Sigma^{(r)} \tag{5a}$$

$$\mathbf{h}_r^{\mathrm{M}} = \begin{bmatrix} \dfrac{(y_k - y_j)}{2A} & 0 & -\dfrac{(x_k - x_j)}{2A} \\[2mm] 0 & -\dfrac{(x_k - x_j)}{2A} & \dfrac{(y_k - y_j)}{2A} \end{bmatrix}$$

$$\mathbf{q}_r^{\mathrm{M}} = \mathbf{h}_r^{\mathrm{M}} \Sigma^{(r)} \tag{5b}$$

where l_{kr} and l_{rj} are the length of the edges connecting nodes kr and rj, respectively ($k = 2,3,1$; $j = 3,1,2$).

Additional constraints on nodal stresses are further imposed in order to enforce prescribed boundary conditions. It is worth underlining that, if boundary conditions are prescribed on two sides of an element, equation (1) provides four constraints on the three internal stress parameters at the corner node that connects these two sides. Therefore, this condition should be avoided in the discretisation

process, otherwise a rank deficiency has to be considered in the factorisation of the equilibrium equation.

The objective of the lower bound approach is to determine the optimal stress distribution that maximizes the external load for a given structure. Inequality constraints are added to the problem, representing the linearised failure surface. The final optimisation problem results in the following linear programming (LP):

$$\max\left\{\begin{bmatrix}\mathbf{0}^T & 1\end{bmatrix}\begin{bmatrix}\boldsymbol{\Sigma} \\ \hat{\boldsymbol{\lambda}}\end{bmatrix}\right\}$$

$$\text{such that}\begin{cases}\mathbf{H}\boldsymbol{\Sigma} + \mathbf{R}\hat{\boldsymbol{\lambda}} = \mathbf{Q} \\ \mathbf{A}^{in}\boldsymbol{\Sigma} \le \mathbf{b}^{in}\end{cases}$$

(5c)

Where $\hat{\boldsymbol{\lambda}}$ is the load multiplier, $\boldsymbol{\Sigma}$ is the vector of (assembled) unknown stress parameters, $\mathbf{H}\boldsymbol{\Sigma} + \mathbf{R}\lambda = \mathbf{Q}$ collects equilibrium of elements, equilibrium on interfaces and boundary conditions, whereas $\mathbf{A}^{in}\boldsymbol{\Sigma} \le \mathbf{b}^{in}$ represents the assembled linearised failure surface.

3   THE UPPER BOUND APPROACH

The upper bound approach developed in this paper is based on the formulation presented in [8] by Sloan and Kleeman. Such formulation is based on a triangular discretization of 2D domains and on the introduction of discontinuities of the velocity field along the edges of adjacent triangles.

For each element E, two velocity unknowns per node i, say u_{xx}^i and u_{yy}^i (one horizontal and one vertical, see Figure 2-a) are introduced, so that the velocity field is linear inside an element, whereas the strain rate field is constant.

Jumps of velocities on interfaces are supposed to vary linearly. Hence, for each interface, four unknowns are introduced ($\Delta\mathbf{u}^I = \begin{bmatrix}\Delta v_1 & \Delta u_1 & \Delta v_2 & \Delta u_2\end{bmatrix}^T$), representing the normal (Δv_i) and tangential

(Δu_i) jumps of velocities (with respect to the discontinuity direction) evaluated on nodes $i = 1$ and $i = 2$ of the interface (see Figure 2-b). For any pair of nodes on the interface between two adjacent triangles $(m) - (n)$, the tangential and normal velocity jumps can be written in terms of the Cartesian nodal velocities of elements $(m) - (n)$ (see [8] for details), so that four linear equations in the form $\mathbf{A}_{11}^{eq}\mathbf{u}^{Em} + \mathbf{A}_{12}^{eq}\mathbf{u}^{En} + \mathbf{A}_{13}^{eq}\Delta\mathbf{u}^I = \mathbf{0}$ can be written for each interface, where $\mathbf{u}^{Em}$ and $\mathbf{u}^{En}$ are the $6x1$ vectorsthat collect velocities of elements (m) and (n) respectively.

It has been shown [8] that the definition of kinematically admissible velocity fields with discontinuities on interfaces is adequate for purely cohesive or cohesive-frictional materials, which is the case of masonry. From a mathematical point of view, it is worth mentioning that the velocity field in the rigid plastic case has to be considered in a functional space larger than the one for the elastic case. Sloan and Kleeman [8] developed an approach for an isotropic material with a Mohr-Coulomb failure surface. Here, a generalisation is developed, with the aim of taking into account the actual shape of the homogenised failure surfaces for interfaces.

For continuum, no modifications are required. Namely, three equality constrains representing the plastic flow in continuum (obeying an associated flow rule) are introduced for each element:

$$\dot{\boldsymbol{\varepsilon}}_{pl}^E = \left[\begin{array}{ccc} \dfrac{\partial u_{xx}}{\partial x} & \dfrac{\partial u_{yy}}{\partial y} & \dfrac{\partial u_{yy}}{\partial x} + \dfrac{\partial u_{xx}}{\partial y} \end{array}\right] = \dot{\lambda}\dfrac{\partial S^{\text{hom}}}{\partial \boldsymbol{\Sigma}}$$, where $\dot{\boldsymbol{\varepsilon}}_{pl}^E$ is the plastic strain rate vector of element

E, $\dot{\lambda} \geq 0$ is the plastic multiplier and S^{hom} is the (non) linear failure surface. Since in the companion paper (Part I), a statically admissible linear approximation (with m planes) of the failure surface has been proposed ($S^{\text{hom}} \equiv \mathbf{A}^{\text{in}}\boldsymbol{\Sigma} \leq \mathbf{b}^{\text{in}}$), three linear equality constraints per element can be written in the form $\mathbf{A}_{11}^{eq}\mathbf{u}^E + \mathbf{A}_{12}^{eq}\dot{\boldsymbol{\lambda}}^E = \mathbf{0}$, where $\mathbf{u}^E$ is the vector of element velocities and $\dot{\boldsymbol{\lambda}}^E$ is a $mx1$ vector of plastic multiplier rates (one for each plane of the linearised failure surface).

For the interfaces, a 2D projection of the 3D failure surfaces is required, which depends on the orientation ϑ of the interface with respect to the horizontal direction.

If a linear approximation of the failure surface is considered (as usually done in the framework of limit analysis, see Part I), for the problem at hand the resulting failure surfaces for interfaces are piecewise linear and generally constituted by m^I segments. They can be easily found once the linearised homogenised failure surface for continuum is provided, for instance through the following optimisation:

$$\begin{cases} \max\{\lambda\} \\ \boldsymbol{\sigma} = \{\sigma_n \quad \tau\}^T = \mathbf{T}\boldsymbol{\Sigma} \\ \mathbf{T} = \begin{bmatrix} \sin^2(\vartheta) & \cos^2(\vartheta) & -\sin(2\vartheta) \\ -\sin(2\vartheta)/2 & \sin(2\vartheta)/2 & \cos(2\vartheta) \end{bmatrix} \\ \sigma_n = \cos(\psi); \ \tau = \sin(\psi) \\ \boldsymbol{\Sigma} \in S^{\text{hom}} \end{cases} \tag{6}$$

where:

- $\boldsymbol{\sigma} = \{\sigma_n \quad \tau\}^T$ is the vector of stress components in the interface;

- $\mathbf{T}$ is the rotation matrix;

- S^{hom} is the (linearised) homogenised failure surface, already introduced in Part I.

- $\psi \in [0;2\pi]$ represents the direction of optimisation in the $\sigma_n - \tau$ plane.

Once the linearised domains for interfaces are provided by means of (6), the power dissipated on the discontinuities is computed introducing plastic multipliers for every interface I as follows:

$$\Delta\mathbf{u}^I(\xi) = \begin{bmatrix} \Delta v^I(\xi) \\ \Delta u^I(\xi) \end{bmatrix} = \sum_{i=1}^{m} \dot{\lambda}_I^{(i)}(\xi)\nabla f_{\boldsymbol{\sigma}}^{(i)} \tag{7}$$

where:

- ξ is the abscissa of I.

- $\nabla f_{\boldsymbol{\sigma}}^{(i)}$ are constant gradients for the failure surface (being $f^{(i)}$, the ith segment of the multi-linear failure surface);

- $\dot{\lambda}_I^{(i)}$ are the interface plastic multiplier rates, evaluated in correspondence of ξ, integrated along the infinitesimal thickness of interfaces and associated with the ith segment of the multi-linear failure surface;

- Δv^I and Δu^I have been already introduced and are respectively the normal and tangential jump of velocities on the discontinuities.

After some elementary assemblage operations, a simple linear programming problem is obtained (analogous to that reported in [8]), where the objective function consists in the minimization of the total internal power dissipated:

$$\begin{cases} \min\left\{ \mathbf{C}_E^T \dot{\boldsymbol{\lambda}}^{E,ass} + \mathbf{C}_I^T \dot{\boldsymbol{\lambda}}^{I,ass} \right\} \\ \text{such that} \begin{cases} \mathbf{A}^{eq}\mathbf{U} = \mathbf{b}^{eq} \\ \dot{\boldsymbol{\lambda}}^{I,ass} \geq \mathbf{0} \\ \dot{\boldsymbol{\lambda}}^{E,ass} \geq \mathbf{0} \end{cases} \end{cases} \tag{8a}$$

where:

- $\mathbf{C}_E^T$ and $\mathbf{C}_I^T$ are the (assembled) right-hand sides of the inequalities which determine the linearised failure surface of the homogenised material respectively in continuum and in the interfaces.

- $\mathbf{U} = \begin{bmatrix} \mathbf{u} & \dot{\boldsymbol{\lambda}}^{E,ass} & \Delta\mathbf{u}^{I,ass} & \dot{\boldsymbol{\lambda}}^{I,ass} \end{bmatrix}$ is the vector of global unknowns, which collects the vector of assembled nodal velocities ($\mathbf{u}$), the vector of assembled element plastic multiplier rates ($\dot{\boldsymbol{\lambda}}^{E,ass}$), the vector of assembled jump of velocities on interfaces ($\Delta\mathbf{u}^{I,ass}$) and the vector of assembled interface plastic multiplier rates ($\dot{\boldsymbol{\lambda}}^{I,ass}$).

- $\mathbf{A}^{eq}$ is the overall constraints matrix and collects velocity boundary conditions, relations between velocity jumps on interfaces and elements velocities, constraints for plastic flow in velocity discontinuities and constraints for plastic flow in continuum.

It is worth noting that $\mathbf{C}_E^T \dot{\boldsymbol{\lambda}}^{E,ass}$ and $\mathbf{C}_I^T \dot{\boldsymbol{\lambda}}^{I,ass}$ in the objective function represent respectively the total power dissipated in continuum and in interfaces. Within each triangle E of area A, supposing (as already pointed out) the homogenised (linearised) failure surface constituted by m planes (of equation $A_{xx}^q \Sigma_{xx} + A_{yy}^q \Sigma_{yy} + A_{xy}^q \Sigma_{xy} = C_E^q \quad 1 \le q \le m$), it can be easily shown that the power dissipated is expressed by the linear equation:

$$P^E = A \sum_{q=1}^m C_E^q \dot{\lambda}_E^{(q)} \tag{8b}$$

where $\dot{\lambda}_E^{(q)}$ is the plastic multiplier rate of the triangle E associated to the qth plane of the linearised failure surface, Figure 2.

In a similar way, within each interface I of length Γ, supposing the homogenised (linearised) strength domain constituted by m^I straight lines (of equation $A_n^{q^I} \sigma_n + A_\tau^{q^I} \tau = C_I^{q^I} \quad 1 \le q^I \le m^I$), the power dissipated is:

$$P^I = \Gamma / 2 \sum_{q=1}^{m^I} C_I^q \left(\dot{\lambda}_{Ii}^{(q)} + \dot{\lambda}_{If}^{(q)} \right) \tag{8c}$$

Where $\dot{\lambda}_{Ii}^{(q)}$ and $\dot{\lambda}_{If}^{(q)}$ represent respectively the qth plastic multiplier rate of the initial (i) and final (f) point of the interface I, being the variation of plastic multiplier rates on interfaces linear.

From a numerical viewpoint, it is worth noting that the overall constraint matrix of the optimisation problem given by equation (8a), reduced in standard form, always has fewer rows than columns. For refined meshes, the ratio of columns to rows in the overall constraint matrix is essentially dependent on the number of planes used in the linearisation of the yield surface (in continuum and

on interfaces). Furthermore, for refined meshes, the density of the overall constraint matrix is very low, i.e. its sparsity becomes larger when the number of elements increases. As suggested by Sloan [7], problems with many elements and refined linearisations of the yield surfaces can be handled using the steepest edge active set algorithm [14] to solve the dual of equation (8). This algorithm provides a very efficient solution strategy and is suited for sparse linear programming problems, with more rows than columns in the constraint matrix.

4 EXAMPLES AND COMPARISONS WITH EXPERIMENTAL DATA

In this Section the accuracy of the results obtained through a homogenised approach is validated through relevant examples from the literature. For a deep beam test and a set of shear walls, both upper and lower bound analyses are dealt with in detail. As it is shown later in the Appendix, convergence of the solutions upon mesh refinement is observed in the analysis and the results do not essentially depend on mesh orientation.

4.1 DEEP BEAM TEST

The first structural example analysed consists in the limit analysis of a masonry panel acting as a deep beam, tested by Page [9]. The wall has a length L equal to 754 mm and a height H equal to 457 mm, being supported at each side over a support length L_s equal to 188 mm, see Figure 3. The top load p, uniformly distributed, is applied through a stiff steel beam. The deep beam was made of half scale pressed solid clay bricks of dimensions 122x37x54 mm^3 and 5 mm thick mortar joints.

The same test has been previously analysed numerically both by Lourenço [15] through an incremental elasto-plastic procedure and by Sutcliffe et al. [11] through a limit analysis approach. In the numerical model proposed by Page [9] the thickness of the mortar is neglected, so reducing

the joints to interfaces. The same simplification is adopted here. Figure 3-b shows the boundary conditions imposed in the lower bound analysis, which include, in free edges, zero normal and zero shear stress, and, in the loading surface, only zero shear stress. No stress boundary conditions are applied at the supports.

In the framework of limit analysis, a linearised frictional-type failure surface is chosen for joints, according to Lourenço and Rots [16] and Sutcliffe et al. [11]. The mechanical characteristics of the joints at failure are shown in Table I. The linearised homogenised failure surface, obtained using the procedure presented in Part I of the paper is shown in Figure 4-a. Furthermore, in Figure 4-b some sections of the 3D surfaces for different orientations of ϑ angle are shown. As it is possible to notice the failure surface is typically orthotropic with low tensile strength, as it usually occurs in masonry.

The structural simulations on the deep beam are handled with a refined linearisation (56 planes) of the homogenised strength domain.

4.1.1 LOWER BOUND APPROACH

The lower bound on the collapse load found is P= 93.5 kN, very close to the experimental collapse load registered by Page (P=109.5 kN) with a percentage error of 14%. In [11], where a micro-mechanical model is adopted (i.e. mortar and units are considered separately taking into account their different failure surfaces), a very satisfactory agreement with the experimental collapse load was found. Nevertheless, as previously discussed, this procedure requires a great computational effort in the optimisation due to the number of variables involved. A complete comparison between experimental data, previously obtained heterogeneous numerical results [11] and results obtained in the present Paper is reported in Table II. Finally, the principal stress distribution provided by the equilibrium model at collapse is shown in Figure 5-a. On the other hand, Figure 5-b shows a

comparison between the vertical stress distribution at 75% of the collapse load provided by the present model in comparison to that by Page [9] (i.e. stresses obtained via limit analysis and LP are reduced in order to compare them with data from literature). Obviously the homogenised approach gives a limit load less than the heterogeneous one. This is mainly a consequence to the fact that both the failure surface is a lower bound approximation of the real one and the brick staggering is taken into account only at a cell level. The two-strut model appearing in the structure that allows the flow of forces from the application edge to the supports is clearly visible, both experimentally and numerically. Finally, it should be underlined that the deviation of the stresses (in comparison both with experimental and incremental numerical procedures, Figure 5-b), provided by the lower bound approach is essentially due to the fact that limit analysis gives meaningful values of stresses only where the material strength is fully utilised (i.e. in the plastic regions).

4.1.2 UPPER BOUND APPROACH

Two different finite element models with discontinuities of velocities on interfaces are here discussed. In the first one (*homogeneous approach*), the micro-mechanical model presented in Part I of this paper has been employed. In the second one (*heterogeneous approach*), specifically developed in this paper, joints and units have been meshed separately, taking into account their different failure surfaces at a structural level. For units, a linearisation with 48 planes of a Mohr-Coulomb failure criterion in plane stress is adopted (cohesion $c = 2 \text{ N/mm}^2$ and friction angle $\varphi = 45°$). It is worth noting that in the upper bound homogeneous approach the failure surface is derived from the equilibrated approach presented in Part I of the paper which obviously represents a non-rigorous lower bound (since failure surfaces of the constituent materials do not fully comply with the requirements for the static admissibility, see Figure 6 Part I). Two different heterogeneous models are tested, the first, with velocity discontinuities only on joints, and the second, where

velocity discontinuities are allowed also on units (i.e. velocity discontinuities also on the interfaces not belonging to a mortar joint are permitted). The introduction of discontinuities on bricks permits to simulate a behaviour more in agreement with the homogenised model, which takes into account the vertical brick staggering only at a cell level. Figure 6 from –a to –c represent the deformed shapes at collapse for the three different models analysed. Figure 6-a and -c are similar and indicate an indentation type of failure, associated mostly to a straight shear crack to the supports and compressive failure at the supports. Figure 6-b exhibits visible locking in the masonry units, which is responsible for additional strength of the deep beam.

The numerical results obtained in terms of collapse load using the discrete and the homogenised models are reported in Table III. As stated above, the heterogeneous model with discontinuities also inside the bricks is kinematically richer and provides better results (rather similar to the homogeneous model).

4.2   SHEAR WALLS

A set of experimental tests on masonry shear walls was carried out by Raijmakers and Vermeltfoort [10]. The width/height ratio (L/H) of the shear walls is 990 /1000 ([mm]/[mm]); the walls were built up with 18 courses of bricks, from which 16 courses were active and 2 were clamped in stiff steel beams, Figure 7. The brick dimensions are 210x52x100 mm^3 and the mortar joints are 10 mm thick. Three different vertical loads (p_1=0.30 N/mm^2; p_2=1.21 N/mm^2; p_3=2.12 N/mm^2) were applied on the top and their resultant was kept constant during the complete loading procedure. The stiff steel beam did not allow rotations of the top and was subsequently pushed with an increasing horizontal force.

Let us underline that the limit load analysis of the present experimental test represents a very difficult task. In the technical literature numerical simulations have been presented under simplified assumptions [11] of the actual experimental set-up and relevant differences between the experimental and limit analysis ultimate load have been obtained for low values of vertical pressure.

In the following, a comparison between the model here proposed and results by Sutcliffe et al. [11] is reported with the sole aim of evaluating the accuracy and the capability of the homogenised method.

4.2.1   LOWER BOUND APPROACH

For the problem at hand, different mechanical properties for joints have been measured experimentally [10] for the different shear walls. Mechanical properties for the joints are reported in Table IV (from [11]). Homogenised failure surfaces for the second and third set of experiments (p_2=1.21 and p_3=2.12 N/mm^2, identical mechanical characteristics for bricks and mortar) have been

already presented in Part I of the paper, while in Figure 8 the homogenised failure surface for the first (p_1 = 0.30 N/mm^2, with slightly changed material parameters) is reported. The structural simulations on the shear walls are handled with a refined linearisation (78 planes) of the homogenised failure surface.

The lower bound approach allows to impose only boundary conditions on stresses. If vertical loads on the top are assumed to be uniform, a significant error could be present on the collapse multiplier, especially for low compressive dead loads. This happens because at very low vertical loads the shear wall may overturn and this failure mechanism, involving mainly horizontal joints with their strength in tension branch, lowers considerably the collapse multiplier and can only be accepted in the simplified analysis carried out here. True experimental boundary conditions preclude rocking failure mechanisms.

In Table V the collapse loads obtained both using the homogenised model here proposed and imposing a uniform vertical pressure on the top (according to [11]) are compared with experimental data and Sutcliffe et al. numerical results [11]. Figure 9 and Figure 10 show respectively the principal stresses distribution and the vertical stress contour, obtained by the optimisation procedure for the three load cases examined. The single strut action to the support, typical of shear walls, is clearly identified in the results. For a higher initially applied vertical load, a plastic region with a significant dimension is found at the compressed toe.

It is worth noting that the overturning of the shear walls can be checked in the framework of the lower bound limit analysis considering the dual optimisation problem, which furnishes the velocities of the barycentre of the elements at collapse. Following Poulsen and Damkilde [13], and Olsen [17] the dual problem can be derived from the primal as follows:

$$
\begin{cases}
\max\{\hat{\lambda}\} \\
\text{such that}
\begin{cases}
\mathbf{H}\boldsymbol{\Sigma} + \mathbf{R}\hat{\lambda} = \mathbf{Q} \\
\mathbf{A}^{in}\boldsymbol{\Sigma} \leq \mathbf{b}^{in}
\end{cases}
\end{cases}
\qquad
\begin{cases}
\min\{\mathbf{Q}^T\mathbf{u} + \mathbf{b}^{in\,T}\boldsymbol{\varphi}\} \\
\text{such that}
\begin{cases}
\mathbf{H}^T\mathbf{u} + \mathbf{A}^{in\,T}\boldsymbol{\varphi} = \mathbf{0} \\
\mathbf{R}^T\mathbf{u} = 1 \\
\boldsymbol{\varphi} \geq \mathbf{0}
\end{cases}
\end{cases}
$$

$$\text{primal} \qquad\qquad\qquad \text{dual} \tag{9}$$

where vector $\mathbf{u}$ contains the velocities of the barycentre of the elements and vector $\boldsymbol{\varphi}$ contains slack variables, with non zero components that identify the active part of the yield surface (see, for instance, Krenk et al. [18]). Furthermore, as recently shown by Olsen in [19], the corresponding dual counterpart is more efficient in terms of time required in the optimisation formulating than the primal problem of equation (9).

For practical applications, a sufficiently correct solution could be found through an iterative procedure applying a distribution of vertical loads with resultant equal to the total external forces, deriving a field of velocities at collapse and finally evaluating an averaged overturning of the top. If overturning is present, a different distribution of loads should be attempted.

In a similar way, an application of a load (for which the resultant is known) on different nodes could be handled within a LP scheme introducing a master node connected to all the nodes on the loading line. In this manner, one equilibrium equation (between the external total load and the nodal stresses integrated) can be written for the loading line.

Finally, it is interesting to note from Figure 11 (where the simplified assumption on boundary conditions here adopted is reported) that the field of velocities at collapse, derived from the dual problem (9) for the case $p = 0.30$ N/mm^2, shows the failure mainly concentrated on horizontal joints. For the problem at hand, this mechanism requires significantly lower loads than those needed to cause diagonal cracking of the panel.

4.2.2 UPPER BOUND APPROACH

The same simplified assumptions on boundary conditions are here accepted for an upper bound limit analysis. In the upper bound formulation, the external power from the variable load is "scaled", fixing it to e.g. 1, whereas a constant load enters in the optimisation when the total external power is evaluated. This means that no constraints are imposed on vertical velocities on the top (Figure 12-a), with the aim to allow overturning and reproduce lower bound numerical simulations by Sutcliffe et al. [11].

In Table VI a comparison between the homogeneous and the heterogeneous model on the collapse load for the three load cases examined is reported. The difference between models in terms of collapse load is very low and the field of velocities, reported for the sake of conciseness only for the first set of shear walls in Figure 12-b (homogeneous upper bound approach) and Figure 12-c (heterogeneous upper bound approach), clearly shows the failure mechanism, fully concentrated on a single horizontal joint, which clearly indicates the rocking type of failure obtained with the lower bound analysis.

5 APPLICATION TO AN OLD MASONRY BUILDING

An inner wall of a five storey building located in Via Martoglio (Catania, Italy), is here analysed. The full geometrical characterisation of the panel with the mesh utilised in the present analysis is reported in Figure 13. 1000 triangular elements are used for the numerical simulation.

The building stands at the corner of Via Martoglio and Via Casoli streets presenting an L shape. The walls at the building perimeter are made of irregular stone masonry while the inner walls, as the one analysed, are made of regular units of dimensions 250x120x55 mm^3 (brick UNI5628/65). The floors are small vaults made of clay brick masonry supported by reinforced concrete girders. The roof is supported by a timber structure. The last storey has a thickness of 120 mm, while the

other storeys have a thickness of 240 mm. The analysed wall is geometrically regular except for the large opening at the centre of the first floor and for a recess at the fifth storey.

The contribution of the RC beams is neglected, supposing the wall constituted only by masonry. The thickness of mortar is neglected in the model, reducing the joints to interfaces. A frictional-type yield surface with cap in compression is chosen (see Part I) for joints, while for units a linear cut-off failure criterion in compression is adopted. Numerical values adopted for joints and bricks, Table VII, are taken according to Brencich et al. [12]. The homogenised failure surface obtained using the micro-mechanical model presented in Part I is shown in Figure 14.

It is interesting to note, for instance from a comparison between Figure 14 and Figure 4, the dependence of the homogenised surface from the mechanical properties of the components and the capability of the model to take into account this dependence. The analysis is performed making use of a linearisation of the homogenised surface with 42 planes. The complete 2D geometrical model of the wall has been meshed by means of an automatic mesh generator (Strand 7™ V.1.05.6) and the discretised geometry has been exported in Matlab-like format to provide a lower and an upper bound limit analysis.

For the lower bound analysis, the seismic load is applied in correspondence of floors by means of an horizontal distributed load of intensity $k_i \lambda$ (k_i constant), where λ is the limit multiplier and k_i, defined in Figure 13, is taken according to the suggestions of the Italian Code ([12]).

Vertical loads, which are independent from the load multiplier, are applied in a similar way in correspondence of the floors, i.e. by means of distributed vertical actions inside the elements. For the sake of simplicity, self weight of masonry is supposed concentrated in correspondence of the floors and added to the remaining dead loads, which are taken according to [12] and [20].

The lower bound analysis gives a total shear at the base of the building of 691 kN, in good agreement with the results obtained in [12] with an incremental procedure ($\cong 750$ kN). Finally in Figure 15 the distribution at collapse of principal membrane actions is reported, with the typical flow of forces in diagonal struts in the piers, associated with combined vertical and horizontal loads. The lower intensity of membrane actions in correspondence of the last storey is due to the reduction of the thickness (one-half with respect to the thickness of the other storeys) and the low loads at the roof level.

In the upper bound analysis, Figure 16, a triangular field of velocities is imposed at every storey, decreasing from the top (where a horizontal velocity $u = 1$ is imposed) to the base (clamped). This choice is in agreement with simulations reported in [20], where a seismic mode I is assumed for the wall. The total shear at the base provided by the upper bound analysis is 787 kN, in good agreement with the results reported in literature. The field of velocity at collapse, Figure 16, clearly shows the cantilever columns mechanism and the failure mainly concentrated on lintels (shear) due to the flexural deformation of the piers.

6   CONCLUSIONS

In the present Paper, the micro-mechanical model presented in Part I by the authors has been applied to the homogenised limit analysis of actual masonry walls.

Meaningful structural examples have been dealt with in detail using both lower and upper bound methods. The reliability of the approach has been shown, for the lower bound case through a comparison with a heterogeneous limit analysis already presented in literature [11] and, for the upper bound case, with a heterogeneous analysis specifically developed by authors.

Finally, an example of an existing masonry building is presented with the aim to show an engineering application of the proposed approach. The approach appears advantageous if compared

with classical incremental procedures, due both to the well known stability of linear programming

schemes and to the very limited computational time required for the simulations.

7 ACKNOWLEDGEMENTS

APPENDIX: MESH INDEPENDENCE STUDY

A mesh dependence study is here reported in the case both of the lower and the upper bound approach. The study is referred to the collapse load of the deep beam test evaluated using different mesh-patterns. Three different mesh-patterns have been considered, namely one crossed triangle mesh and two preferentially oriented triangular meshes, and four mesh sizes have been considered for each mesh-pattern, as shown in Figure 17. The results obtained using respectively a lower and an upper bound analysis, with and without discontinuities, are also reported in Figure 17. Two aspects are particularly worth noting, the first is referred to the convergence to a unique value for sufficiently refined meshes, the second is related to the higher accuracy of the upper bound approach with discontinuities on interfaces in comparison with a continuous one.

REFERENCES

[1] Lourenço PB, de Borst R, Rots JG. A plane stress softening plasticity model for orthotropic materials. International Journal for Numerical Methods in Engineering 1997; 40: 4033-4057.

[2] Gambarotta L, Lagomarsino S. Damage models for the seismic response of brick masonry shear walls. Part II: the continuum model and its applications. Earthquake Engineering and Structural Dynamics 1997; 26: 441-462.

[3] Zucchini A, Lourenco PB. A micro-mechanical model for the homogenisation of masonry. International Journal of Solids and Structures 2002; 39: 3233-3255.

[4]   Suquet P. Analyse limite et homogeneisation. C.R. Acad. Sci., Paris 1983; 296 (Serie II): 1355-1358.

[5]   de Buhan P, de Felice G. A homogenisation approach to the ultimate strength of brick masonry. Journal of the Mechanics and Physics of Solids 1997; 45 (7): 1085-1104.

[6]   Orduna A. Seismic assessment of ancient masonry structures by rigid blocks limit analysis. PhD Thesis 2003. University of Minho, Portugal. Available at www.civil.uminho.pt/masonry.

[7]   Sloan SW. Lower bound limit analysis using finite elements and linear programming. International Journal for Numerical and Analytical Methods in Geomechanics 1988; 12: 61-77.

[8]   Sloan SW, Kleeman PW. Upper bound limit analysis using discontinuous velocity fields. Computer Methods in Applied Mechanics and Engineering 1995; 127 (1-4): 293-314.

[9]   Page AW. Finite element model for masonry. Journal of Structural Division ASCE 1978; 104(8): 1267-1285.

[10] Raijmakers TMJ, Vermeltfoort A. Deformation controlled tests in masonry shear walls (in Dutch). Report B-92-1156, TNO-Bouw, Delft, The Netherlands, 1992.

[11] Sutcliffe DJ, Yu HS, Page AW. Lower bound limit analysis of unreinforced masonry shear walls. Computers and Structures 2001; 79: 1295-1312.

[12] Brencich A, Gambarotta L, Lagomarsino S. Catania Project: Research on the seismic response of two masonry buildings. Chapter 6: Analysis of a masonry building in Via Martoglio. University of Genoa (in Italian). CNR Gruppo Nazionale per la Difesa dei Terremoti 2000; 107-151.

[13] Poulsen PN, Damkilde L. Limit state analysis of reinforced concrete plates subjected to in-plane forces. International Journal of Solids and Structures 2000; 37: 6011-6029.

[14] Sloan SW. A steepest edge active set algorithm for solving sparse linear programming problems. International Journal Numerical Methods Engineering 1988; 12: 61-67.

[15] Lourenço PB. Computational strategies for masonry structures. PhD Thesis 1996. Delft University of Technology, the Netherlands. Available at www.civil.uminho.pt/masonry.

[16] Lourenço PB, Rots J. A multi-surface interface model for the analysis of masonry structures. Journal of Engineering Mechanics ASCE 1997; 123 (7): 660-668.

[17] Olsen PC. Rigid-plastic finite element analysis of steel plates, structural girders and connections. Computer Methods in Applied Mechanics and Engineering 2001; 191: 761-781.

[18] Krenk S, Damkilde L, Hoyer O. Limit analysis and optimal design of plates with triangular equilibrium elements. Journal of Engineering Mechanics 1994; 120(6): 1237-1254.

[19] Olsen PC. Evaluation of triangular elements in rigid-plastic finite element analysis of reinforced concrete. Computer Methods in Applied Mechanics and Engineering 1999; 179: 1-17.

[20] Magenes G, Braggio C. Catania Project: Research on the seismic response of two masonry buildings. Chapter 7: Analysis of a masonry building in Via Martoglio. University of Pavia (in Italian). CNR Gruppo Nazionale per la Difesa dei Terremoti 2000; 153-190.

LIST OF FIGURES:

Figure 1: Lower bound triangular element by Sloan [7] with linear variation of stresses; -a: continuity of the stress vector on interfaces. –b: variation of stresses inside an element

Figure 2: Triangular element used in the upper bound FE limit analysis (-a) and jump of velocities on interfaces between adjacent triangles (-b).

Figure 3: Geometry and loads for the deep beam test proposed by Page [9] (-a) and lower bound boundary conditions applied (-b).

Figure 4: Homogenised failure surface for the deep beam test in the space of homogenised membrane stresses (-a) and for different values of ϑ angle (-b). Here, Σ_h and Σ_v are the principal stresses.

Figure 5: Principal stresses distribution at collapse for the deep beam test (-a) and contour plot of vertical stress distribution in the deep beam test at 75% of collapse load (-b). The stress is averaged on common nodes.

Figure 6: Field of velocities at collapse for the deep beam test, upper bound approach. -a: homogenised approach; -b: heterogeneous approach with discontinuities only on mortar interfaces; -c: heterogeneous approach with discontinuities both on mortar and unit interfaces.

Figure 7: Geometry and loading of shear wall of Raijmakers and Vermeltfoort [10].

Figure 8: Homogenised failure surface in the space of homogenised membrane stresses; shear walls, vertical load p=1.21 N/mm^2 and 2.12 N/mm^2.

Figure 9: Principal stresses distribution for the set of shear walls. -a: p=0.30 N/mm^2; -b: p=1.21 N/mm^2; -c: p=2.12 N/mm^2. The stress is averaged on common nodes.

Figure 10: Vertical stress contour (N/mm^2) for the set of shear walls. -a: p=0.30 N/mm^2; -b: p=1.21 N/mm^2; -c: p=2.12 N/mm^2. The stress is averaged on common nodes.

Figure 11: Field of velocities at collapse from the lower bound problem and simplified boundary conditions imposed, for the shear test wall with p=0.30 N/mm^2.

Figure 12: Shear wall (p=0.30 N/mm^2) analysed with the upper bound approach. -a: simplified boundary conditions assumptions of the experimental set-up; -b: field of velocities at collapse for the homogeneous approach; -c: field of velocities at collapse for the heterogeneous approach.

Figure 13: Via Martoglio wall: geometry (in cm), mesh utilised and seismic load applied for the lower bound analysis.

Figure 14: Homogenised failure surface for the Via Martoglio wall in the space of homogenised membrane stresses.

Figure 15: Distribution at collapse of principal membrane actions from the lower bound analysis.

Figure 16: Deformed shape at collapse for the upper bound analysis.

Figure 17: Mesh dependence plot for the deep beam test.

Homogenisation approach: $b_x = b_y = 0$

continuity of the stress vector between adjacent elements

linear variation of stresses inside an element

$\mathbf{b} = [b_x \; b_y]^T$

-a

-b

Figure 1

linearised homogenized failure surface (S^{hom})

$\dot{\varepsilon}_{pl}^E = \dot{\lambda}_E^{(q)} \dfrac{\partial S^{\text{hom}}}{\partial \Sigma}$

plane

$A_{xx}^q \Sigma_{xx} + A_{yy}^q \Sigma_{yy} + A_{xy}^q \Sigma_{xy} = C_E^q$

$\mathbf{3}(u_{xx}^3; u_{yy}^3)$

$\mathbf{2}(u_{xx}^2; u_{yy}^2)$

$\mathbf{1}(u_{xx}^1; u_{yy}^1)$

$\dot{\boldsymbol{\lambda}} = (\dot{\lambda}_E^{(1)}; \dot{\lambda}_E^{(2)}; \dots; \dot{\lambda}_E^{(m)})$

(n) element

(m) element

$(u_{xx}^{2(n)}; u_{yy}^{2(n)})$

$(u_{xx}^{2(m)}; u_{yy}^{2(m)})$

$(u_{xx}^{1(n)}; u_{yy}^{1(n)})$

$(u_{xx}^{1(m)}; u_{yy}^{1(m)})$

Δv

Δu

ϑ^i

$\mathbf{n}$

$\mathbf{n}$: normal to the interface

-a

-b

Figure 2

-a

-b
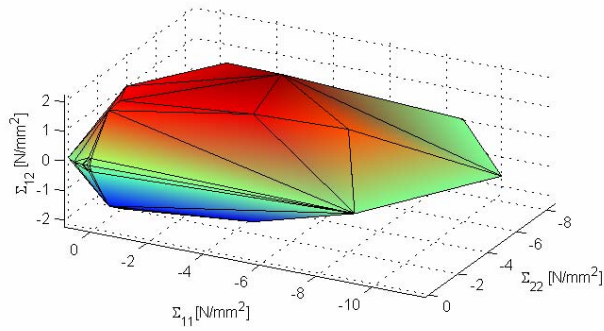
Figure 3

-a
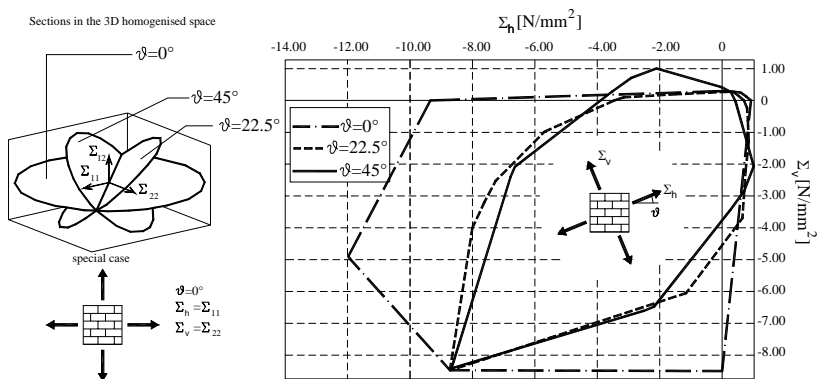
-b

Figure 4

-a

-b

Figure 5

-a   -b   -c

Figure 6

Figure 7

Figure 8

Mesh

-a   -b   -c

Figure 9

33

-a   -b   -c
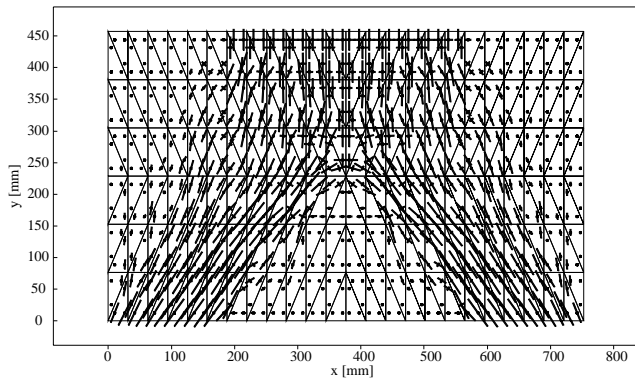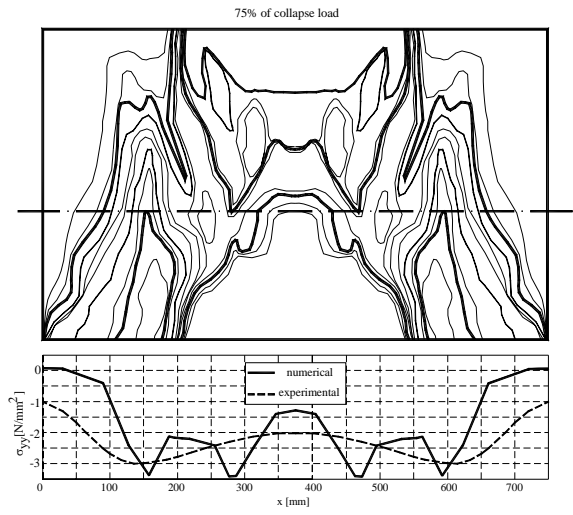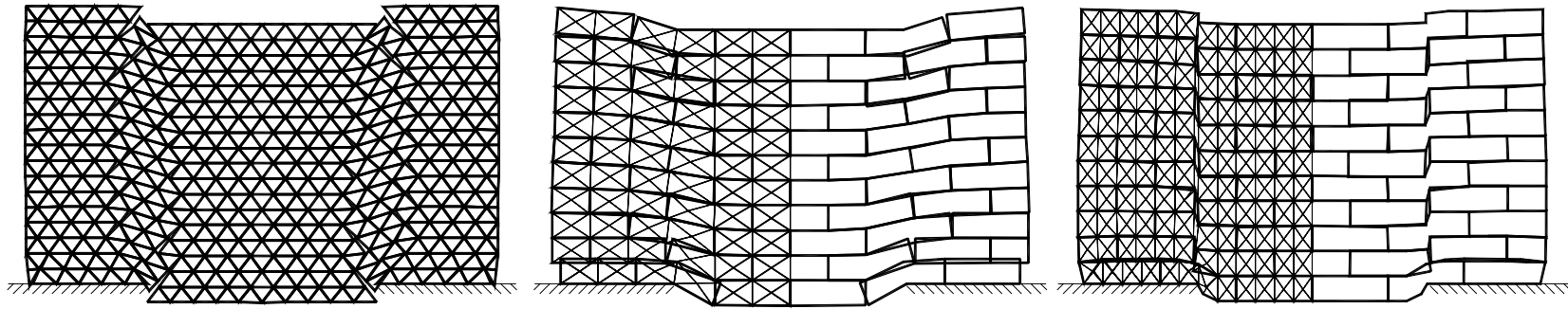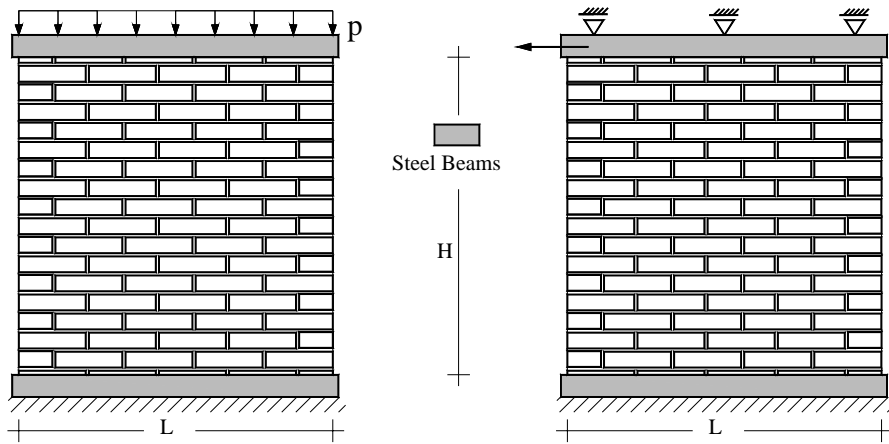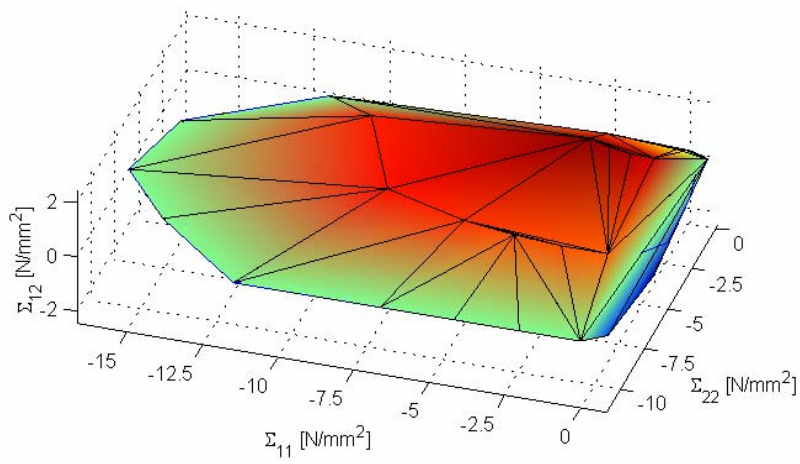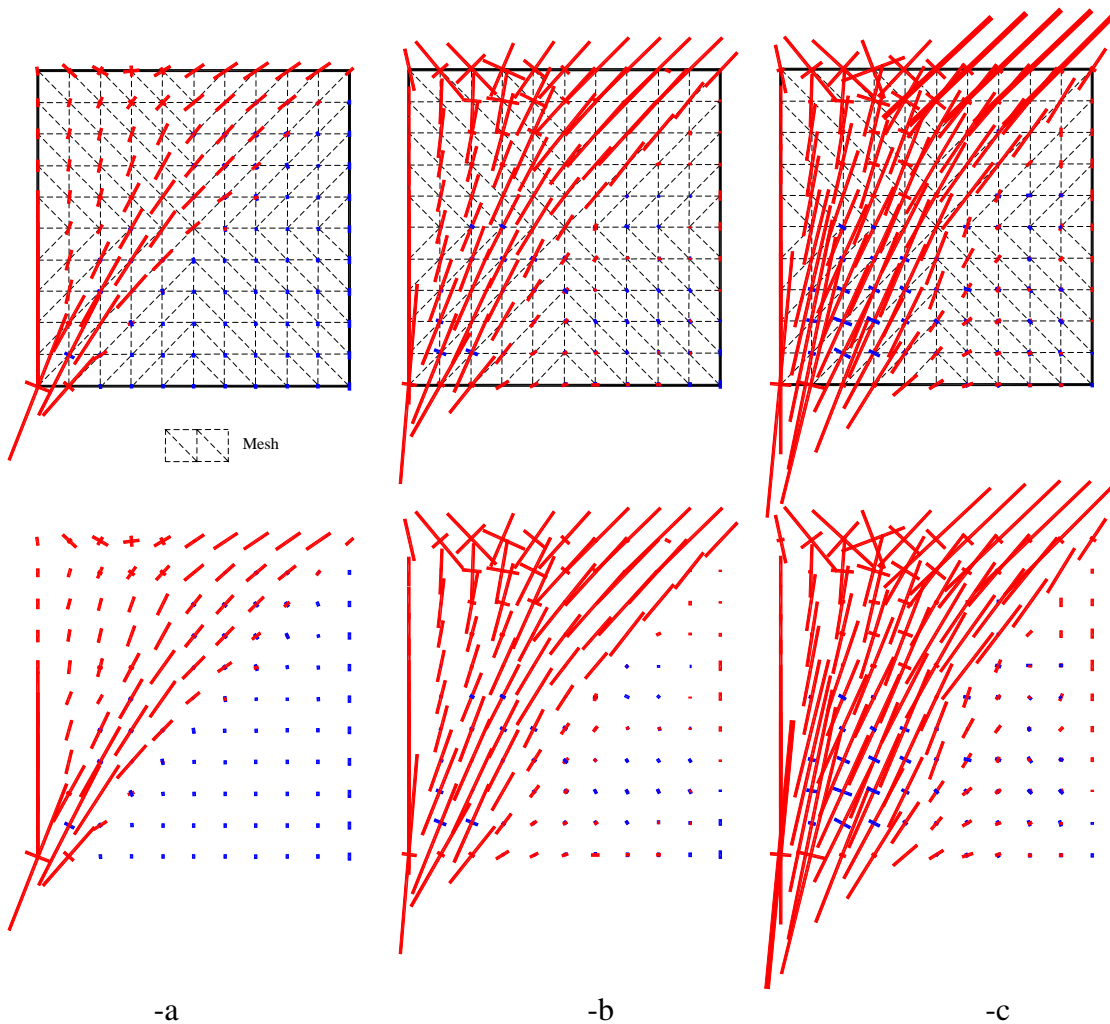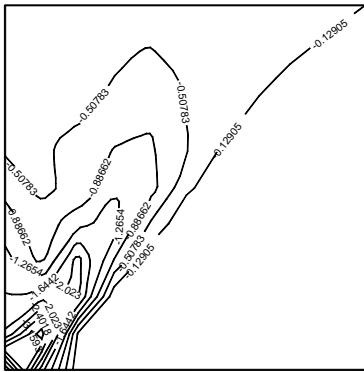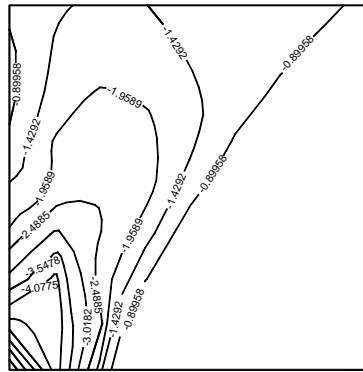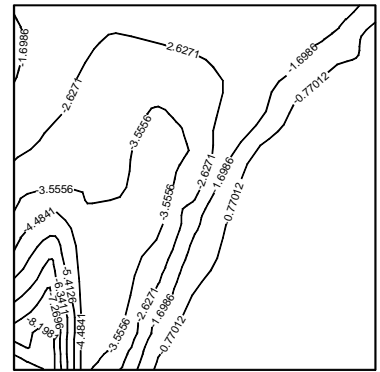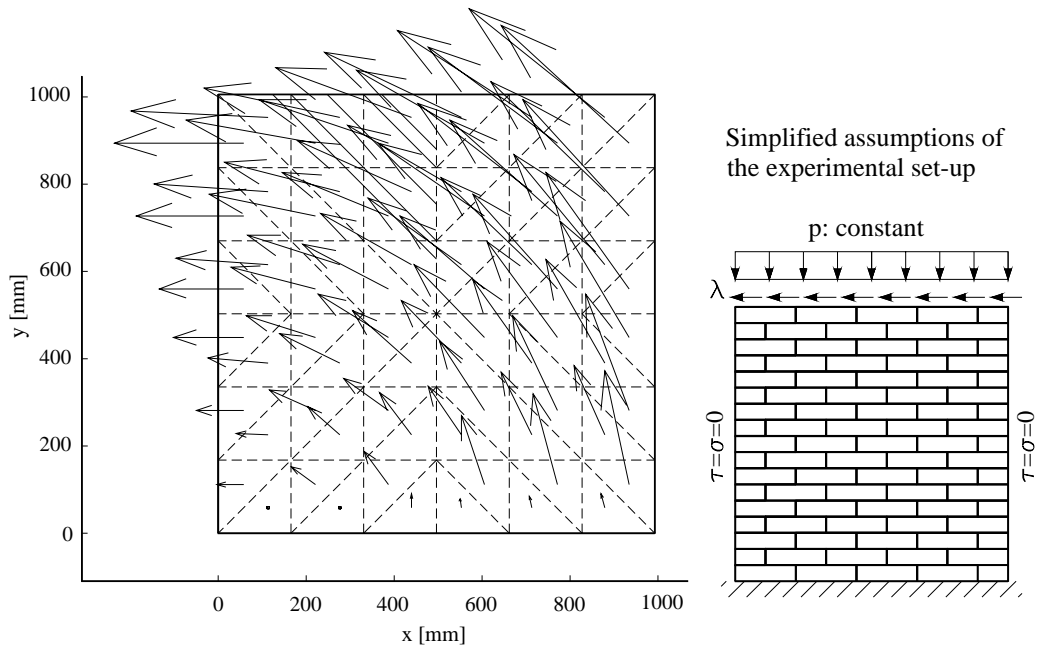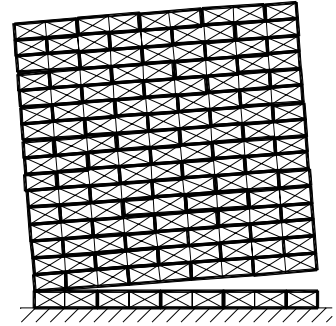
Figure 10

Figure 11

Simplified assumptions of
the experimental set-up

p: constant

u=-1

v

u

u=v=0
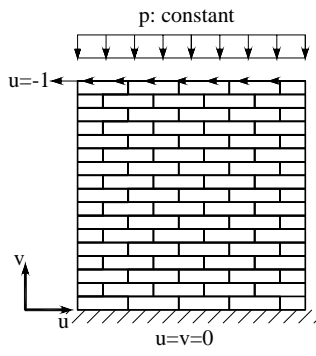
number of elements: 72
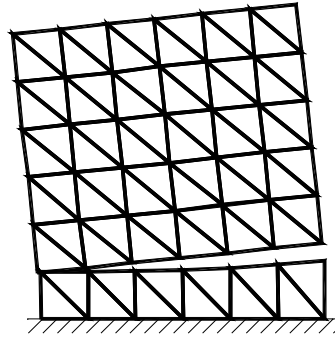
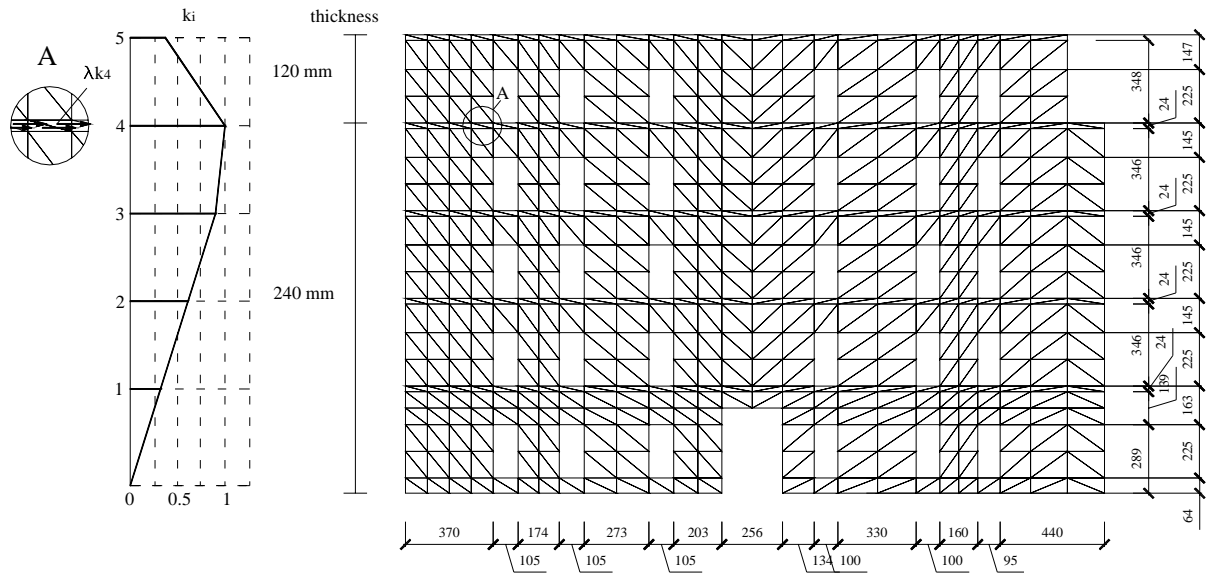number of elements:
bricks: 612
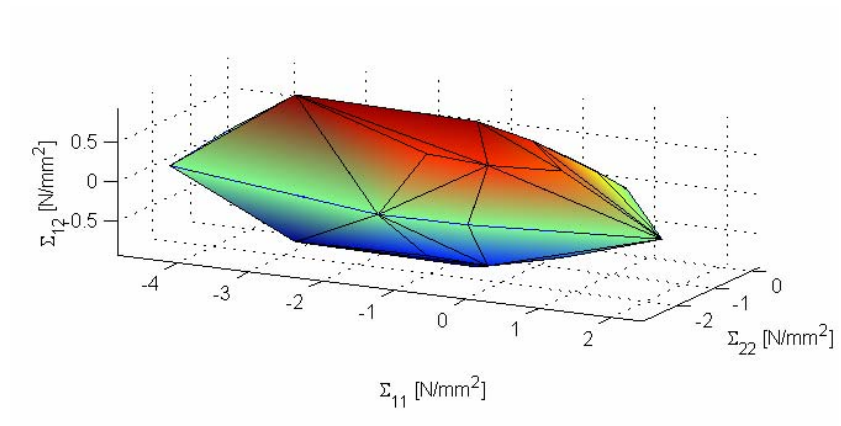mortar interfaces: 212

-a

-b

-c

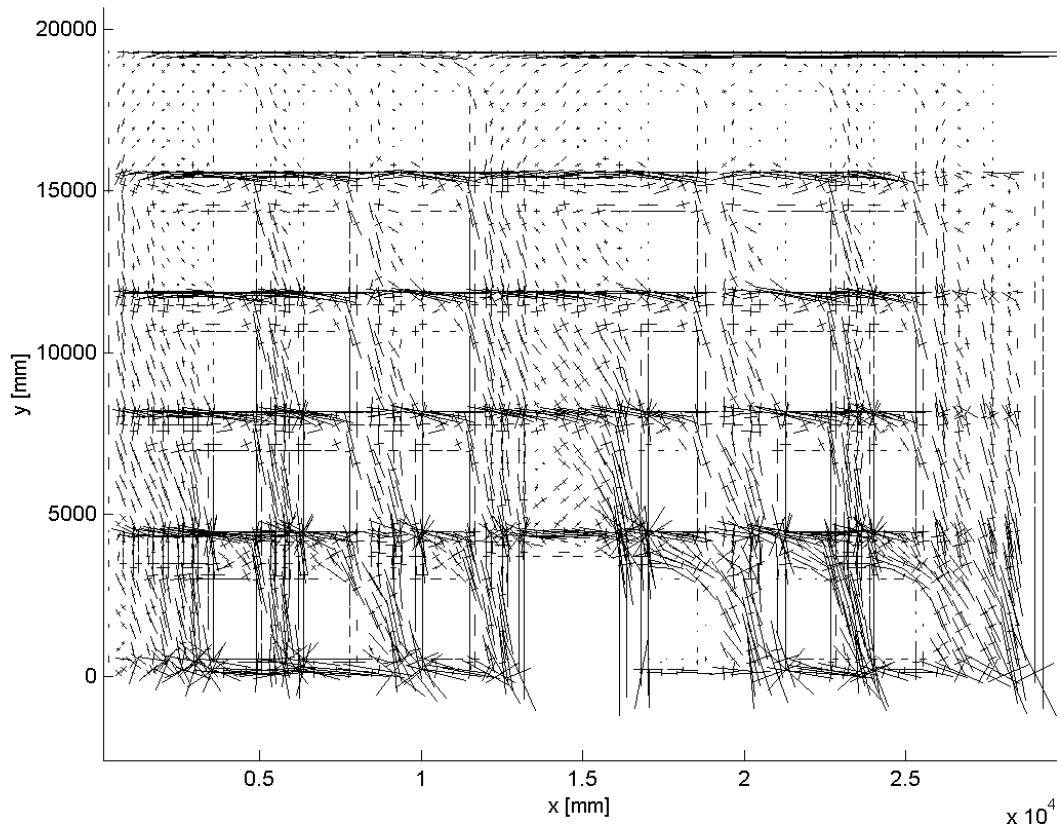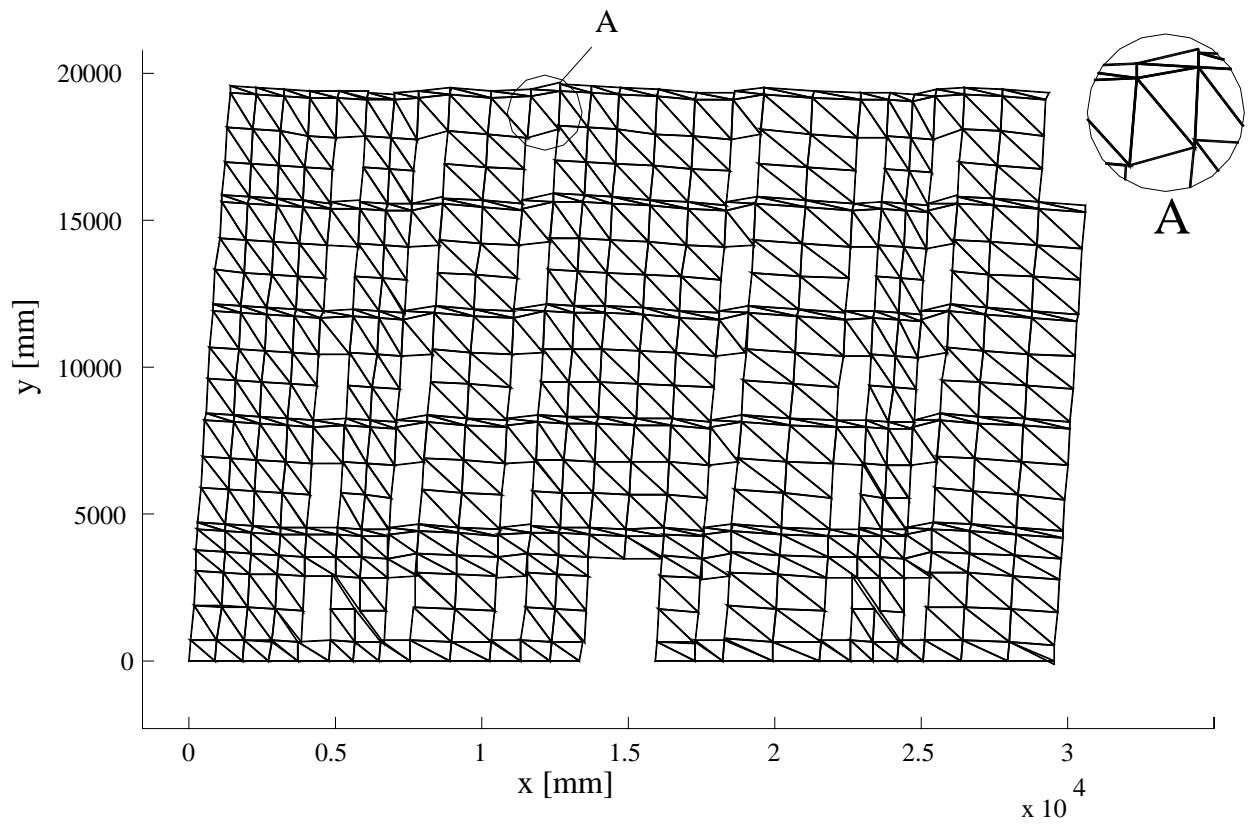Figure 12
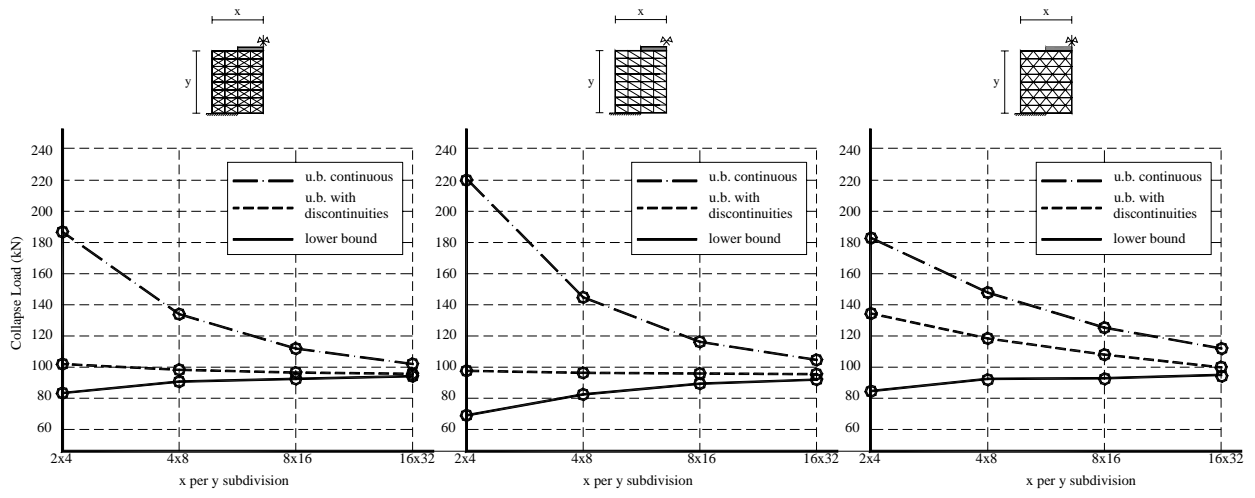
Figure 13

Figure 14

Figure 15

Figure 16

Figure 17

41

LIST OF TABLES:

Table I: Interface mechanical properties for joints in the deep beam test. A Mohr-Coulomb failure criterion with tension cut-off and linearised cap in compression is adopted, see Part I of the paper. Here, f_t is the tensile strength, f_c is the compressive strength, c is the cohesion, Φ_1 is the friction angle and Φ_2 represents the linearised shape of the compressive cap.

Table II: Comparison among collapse loads obtained through a lower bound homogeneous approach, a lower bound heterogeneous approach and experimental data (deep beam test).

Table III: Comparison among collapse loads obtained through an upper bound homogeneous approach, an upper bound heterogeneous approach with discontinuities of the velocity field on joints and bricks and an upper bound heterogeneous approach with discontinuities of the velocity field only on joints (deep beam test).

Table IV: Interface mechanical properties for joints in the shear wall tests. A Mohr-Coulomb failure criterion with tension cut-off and linearised cap in compression is adopted, see Part I of the paper. Here, f_t is the tensile strength, f_c is the compressive strength, c is the cohesion, Φ_1 is the friction angle and Φ_2 represents the linearised shape of the compressive cap.

Table V: Comparison among collapse loads obtained through a lower bound homogeneous approach, a lower bound heterogeneous approach and experimental data (set of shear walls).

Table VI: Comparison between collapse loads obtained through an upper bound homogeneous approach and an upper bound heterogeneous approach (set of shear walls).

Table VII: Mechanical properties of joints and bricks of Via Martoglio wall. For joints, a Mohr-Coulomb failure criterion with tension cut-off and linearised cap in compression is adopted, see Part I of the paper. Here, f_t is the tensile strength, f_c is the compressive strength, c is the cohesion, Φ_1 is the friction angle and Φ_2 represents the linearised shape of the compressive cap.

f_t [N/mm^2]	f_c [N/mm^2]	Φ_1	Φ_2	c [N/mm^2]
0.29	8.6	37°	30°	1.4 f_t

Table I

	Collapse Load [kN]	Number of elements
Homogenous approach	93.5	288 (mesh 24x6)
Heterogeneous approach [11]	105.2	708(*)
Experimental	109.2	-

(*)interfaces included
Table II

	Collapse Load [kN]	Number of elements
Homogeneous approach	115.9	400 (mesh 20x10)
Heterogeneous approach with discontinuities on units and joints	117	1056(*)
Heterogeneous approach without discontinuities on units	148	528 (*)

(*)interfaces excluded

Table III

Vertical load p [N/mm^2]	f$_t$ [N/mm^2]	f$_c$ [N/mm^2]	Φ_1	Φ_2	c [N/mm^2]
0.30	0.25	10.5	37°	30°	1.4 f$_t$
1.21 & 2.12	0.16	11.5	37°	30°	1.4 f$_t$

Table IV

Vertical load p [N/mm^2]	Collapse Load [kN]		
	Homogeneous approach	Heterogenous approach [11]	Experimental
0.30	24.22	26.5	50
1.21	54.63	57.5	72
2.12	80.81	82.9	97

Table V

| | Collapse Load [kN] | |
Vertical load p [N/mm^2]	Homogeneous approach	Heterogeneous approach
0.30	30.71	27.75
1.21	65.12	61.20
2.12	90.66	88.68

Table VI

		Joint			Unit
c [N/mm^2]	f_t [N/mm^2]	f_c [N/mm^2]	Φ_1	Φ_2	f_c [N/mm^2]
0.15	0.1	6	27°	90°	3

Table VII